Three-dimensional thermohaline anomaly structures of rings in the Kuroshio Extension region

Ya'nan Ding[1], Chunsheng Jing[1]*

[1] Third Institute of Oceanography, Ministry of Nature Resources, Xiamen 361005, China

Abstract

Using AVISO satellite altimeter observations during 1993–2015 and a manual eddy detection method, a total of 276 anticyclonic rings and 242 cyclonic rings shed from the Kuroshio Extension (KE) were identified, and their three-dimensional (3D) anomaly structures were further reconstructd based on the Argo float data and the Japan Agency for Marine-Earth Science and Technology (JAMSTEC) cruise and buoy data through an interpolation method. It is found that the cyclonic (anticyclonic) rings presented consistent negative (positive) anomalies of potential temperature; meanwhile the relevant maximum anomaly center became increasingly shallow for the cyclonic rings whereas it went deeper for the anticyclonic rings as the potential temperature anomaly decreased from the west to the east. The above deepening or shoaling trend is associated with the zonal change of the depth of the main thermocline. Moreover, the composite cold ring between 140° and 150°E was found to exhibit a double-core vertical structure due to the existence of mode water with low potential vorticity. Specifically, a relatively large negative (positive) salinity anomaly and a small positive (negative) one appeared for the composite cyclonic (anticyclonic) ring at the depth above and below 600 m, respectively. The underlying driving force for the temperature and salinity anomaly of the composite rings was also attempted, which varies depending on the intensity of the background current and the temperature and salinity fields in different areas of the KE region, and the rings' influences on the temperature and salinity could reach deeper than 1 000 m on average.

Key words: Kuroshio Extension, pinched-off ring, thermohaline anomaly, three-dimensional structure, composite eddy

---

1 Introduction

After separating from the Japan coast near 35°N, the Kuroshio enters the open North Pacific where it is named as the Kuroshio Extension (KE) (32°–38°N, 140°–180°E) (Qiu, 2000). Free from the constraint of coasts, the Kuroshio Extension becomes an eastward-flowing inertial jet, accompanied by large-amplitude meanders and energetic pinched-off eddies (Olson, 1991; Qiu, 2003). These eddies shed from the KE jet due to the instability mechanism are also called "rings" (Olson, 1991).

A ring carries all the characteristics of its source, and can move hundreds or even thousands of kilometers over its life time of months or even years. It plays important roles in eddy transports of heat and salt (Jochumsen et al., 2010; Souza et al., 2015). It eliminates the energy from the jet and reduces the potential vorticity gradient associated with the jet (Olson, 1991), but may also reinforce the jet via momentum convergence (Waterman and Hoskins, 2013). The three-dimensional (3D) structures of the rings are particularly interesting, as they are of paramount importance in regulating the eventual ecological or hydrodynamical influences of the ring on the relevant region. For instance, the cyclonic ring is often accompanied by a strong upwelling structure (Martin and Richards, 2001); as a result, the nutrients would be vertically transported into the euphotic zone, which are im-

portant for the marine ecosystems. In addition, one important impact of rings on the regional ocean condition is producing temperature and salinity anomalies through vertical movements, which can propagate to remote regions via the ocean circulation (Zhang et al., 1998). Such effect could be revealed by comparing the eddy-involved profiles against the climatologic mean state (Roemmich and Gilson, 2001). However, previous studies did not distinguish pinched-off rings very well from meanders of the jet and other mesoscale eddies (Chelton et al., 2007; Itoh and Yasuda, 2010; Kouketsu et al., 2012). As a matter of fact, the ring tends to trap water mass in its interior region compared with weak eddies (Mcwilliams and Flierl, 1979; Chelton et al., 2011) and meanders of the jet (Cushman-Roisin, 1993); and they also assume different propagation tendency and upwelling structures from the meanders (Cushman-Roisin, 1993; McGillicuddy et al., 2007).

To reveal the underlying spatial and/or temporal attributes of the rings, different detection methods have been developed in this regard. Sasaki and Minobe (2015) used a jet length change detection method to track rings shed from the KE jet, and then examined the climatological mean features of these rings; according to their rough estimation, the meridional heat transport across the KE jet by these rings was around 0.023 PW. Neverthe-

less, in their study the KE jet was simply assumed as a single jet which only took the main branches of the bifurcated currents into consideration, as a consequence of which the population of the rings formed was actually underestimated. Recently, a Winding-Angle (WA) eddy detection method was deployed by Ding et al. (2019) to manually identify rings using the AVISO satellite altimeter observations, which enabled them to examine the spatial distribution characteristics, the motion properties, and the seasonal, interannual, and decadal variations of these rings. Chaigneau et al. (2008) and Yang (2013) compared the results yielded by a variety of detection methods and concluded that the WA detection algorithm has a higher chance for successful detection of the mesoscale eddies, more importantly, with a much smaller detection error.

Meanwhile, in recent years, satellite altimeter data, hydrological in-situ data, and Argo float profile data have been employed simultaneously to analyze the statistical characteristics and 3D structures of mesoscale eddies. Chaigneau et al. (2011) investigated the mean vertical structure of mesoscale eddies in the Peru-Chile Current System by combining the historical records of Argo float profiles and satellite altimetry data; the volume, heat, and salt transports caused by eddies were estimated. Yang et al. (2013) used the WA tracking method and Argo float profiles to obtain the composited 3D structures of eddies in the northwestern subtropical Pacific Ocean. Dong et al. (2017) used the FAG algorithm (Faghmous et al., 2015) along with satellite data and Argo profiles to investigate 3D structures and transports of mesoscale eddies in the KE region. Such FAG algorithm focuses on an SLA-based method that detects eddies independent of their trapping ability. Regardless of these numerous relevant studies, nevertheless, research on the 3D structures of the rings shed from the KE jet have never been carried out to the best of our knowledge.

In this paper, the rings shed from the KE jet were identified comprehensively, and their 3D thermohaline anomaly structure were reconstructed. The paper is organized as follows. In Section 2, we describe the data and present the identification algorithm of rings from satellite data as well as the methodology used to classify the Argo profiles. The methodology used for constructing the 3D composite rings is presented in Section 3, which reveals the mean thermohaline anomaly properties of the composite rings. In Section 4, we summarize and discuss the main findings of this study.

2 Data and methods

2.1 *Satellite altimeter data*

The Absolute dynamic topography (ADT) data used in this study are from the gridded multi-mission sea surface altimeter product from January 1993 to December 2015, provided by the Ssalto/Duacs and distributed by the Archiving, Validation, and Interpretation of Satellite Oceanographic data (AVISO) project. These merged data are based on the TOPEX/Poseidon, European Remote Sensing Satellite-1 (ERS-1) and ERS-2, Geosat Follow-On, and Jason-1/Jason-2 along-track satellite altimeters. The ADT data used here represent the sum of the sea level anomaly (SLA) and the mean dynamic topography (MDT), with spatial and temporal resolutions of 0.25°×0.25° and 1 day, respectively. Such high-resolution data provide us with a powerful tool to monitor the mesoscale eddy signals. Compared with SLA data, ADT data retain the sea surface height (SSH) signal affected by a background current over a long-time scale, which hence work

better for identification of the rings shed from the KE jet.

2.2 *Argo profiles and WOA13 climatology*

Accumulation of the Argo profiles in the past decade provides a large amount of subsurface temperature/salinity records, which can be used for reconstructing the relevant 3D structures. The Argo profile data from May 1998 to December 2015 were obtained from the French Research Institute for Exploitation of the Sea (Ifremer; ftp://ftp.ifremer.fr/ifremer/argo/geo). These profiles have gone through automatic preprocessing and quality control procedures at the Argo data center. In our study, only those ascending records with a quality flag of 1, which indicates "good" quality are used. More stringent conditions were adopted for further quality control. Specifically, following Chaigneau et al. (2011) and Yang et al. (2013), data used in this research also meet with the following conditions: (1) the shallowest data shall be located from the surface down to the depth of 10 m, and the deepest acquisition shall be below 1 000 m; (2) the number of data levels from the depth of 0 to 1 000 m shall be larger than 30; and (3) the pressure profile must increase monotonically with depth. Then, An extensive manual checking and editing was performed on all the profiles; any suspicious profiles with potential errors in temperature or salinity records were discarded.

To obtain the thermohaline anomaly structures of the rings, the potential temperature anomaly and the salinity anomaly of the Argo profiles were computed by removing climatologic profiles. The climatologic fields originate from the World Ocean Atlas 2013 v2 dataset produced by the Ocean Climate Laboratory of NOAA's National Oceanographic Data Center; they are on 0.25°×0.25° grid with standard levels.

2.3 *Cruise and buoy data*

The cruise conductivity-temperature-depth (CTD) profile data are from the Japan Agency for Marine-Earth Science and Technology (JAMSTEC, 2016). On 18 February 2007, at 37°–55.33°N ,146°–34.64°E, (nominal 38.0°N, 146.5°E, named as "JAMSTEC Kuroshio Extension Observatory, JKEO" site) north of the KE region, the Institute of Observational Research For Global Change study project (IORGC) of JAMSTEC deployed a surface buoy (JKEO) in collaboration with the Pacific Marine Environmental Laboratory (PMEL) of NOAA. This JKEO buoy is based on the KEO buoy of NOAA/PMEL and carries the same sensors as the KEO to monitor heat, moisture, and momentum fluxes, as well as the upper-ocean temperature and salinity.

2.4 *Eddy detection and tracking methods*

Our manual identification involved with the usage of the WA method, based on our previous work (Ding et al., 2019). A ring is thought to come into being if the enclosed ADT contour with a positive (negative) ADT center is found within the eddy and the diameter of its outermost contour is larger than 100 km. In cases where the ADT contours of the eddy are totally disconnected from those of the KE jet, the eddy are deemed as detached or shed from the KE jet (Fig. 1). In this study, only rings with lifespan longer than two weeks were retained for further analysis, with the lifespan defined as the duration between its shedding point and demising point.

A total of 276 anticyclonic rings and 242 cyclonic rings are identified in our study area (28°–42°N, 135°–180°E), with a mean lifespan of 50 d. The modal radius and the mean amplitude are 92.4 km and 35 cm for the cyclonic rings, 103.9 km and 32 cm for the anticyclonic, respectively, which are similar to those reported by Sasaki and Minobe (2015).
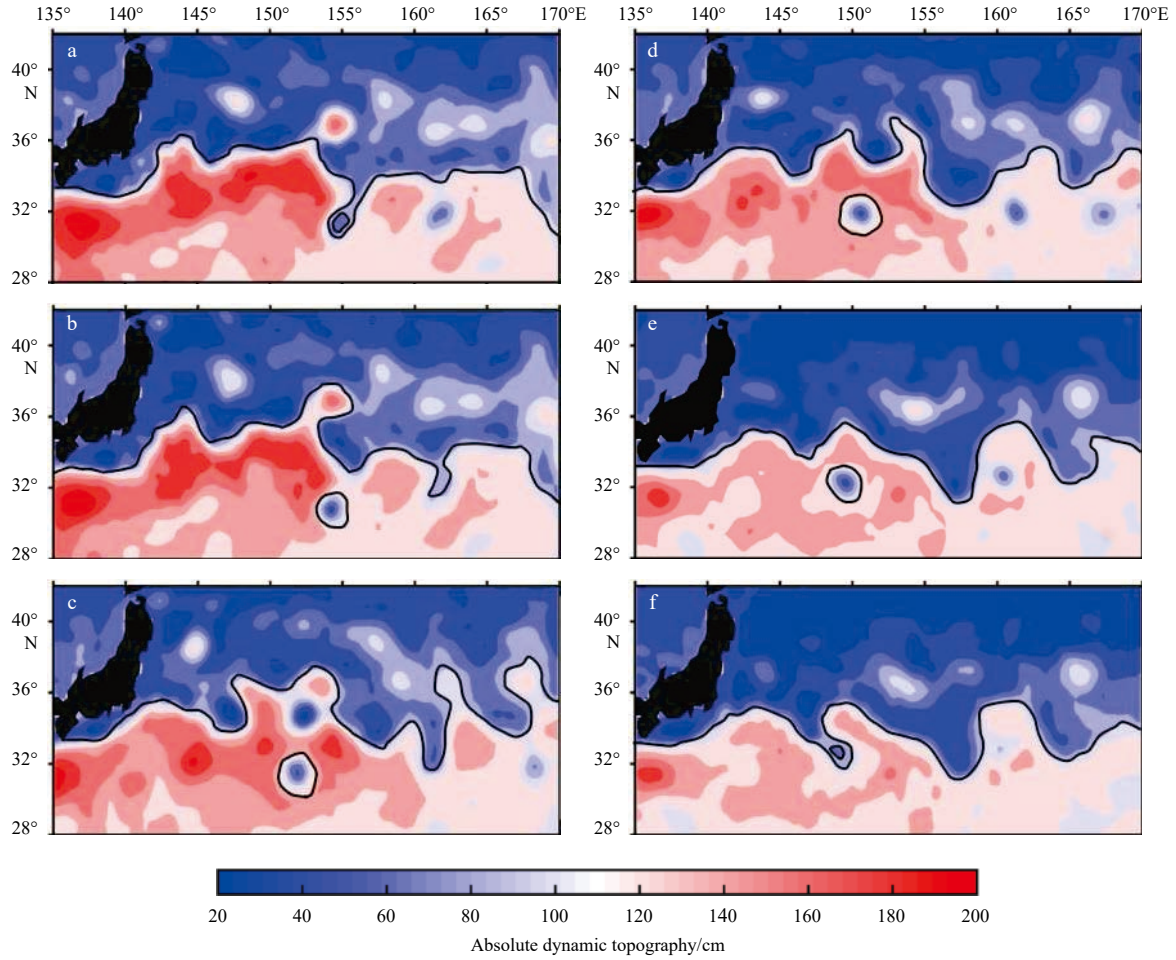
Fig. 1. An example of a cyclonic ring shed from the Kuroshio Extension (KE) jet at (31.0°N, 154.5°E). a–f. The temporal evolution of this cyclonic ring from 16 September 2005 to 23 January 2006, respectively. Color indicates absolute dynamic topography (cm), and black contour the path of the KE axis and the pinched-off ring.

3 Three-dimensional structures

To capture the zonal differences of the ring structures, five sub-regions in consecutive longitude segments are defined as below: Region A (135°–140°E), Region B (140°–150°E), Region C (150°–160°E), Region D (160°–170°E), and Region E (170°E–180°) (Fig. 2a). Statistics of the rings shed from the KE jet during the period 1993–2015 are shown from region B to E in Table 1. Note that the sub-region A is not included since there was only one single ring formed which yet was splitted into two parts by the land in this region.

Prior to discussions on the composite ring structures, the main water masses in the study regions shall be introduced, since our study reveals that the water mass stratification is an essential factor in determining the ring structure. As shown in Fig. 2b, all the mean θ/S diagrams of the four sub-regions show a reversed "S" shape, with two salinity extrema featuring two important water masses, that is, the high-salinity North Pacific Tropical Water (NPTW) of less than 25.5 σ_θ (Suga et al., 2000) and the low-salinity North Pacific Intermediate Water (NPIW, S<34.2) between 26.6 and 27.1 σ_θ (Talley and Lynne, 1993). Beneath the NPTW, the low potential vorticity (PV) North Pacific Subtropical Mode Water (STMW) exists within the main thermocline (Masuzawa, 1969; Suga et al., 2010), which splits the main thermocline into an upper and a lower portion. Signatures of the STMW are the most evident in sub-region B with its PV minimum located at the

depth between 250 and 350 m (Fig. 2c).

3.1 *Construction method*

For each Argo float selected and all cruise CTD profiles, their temperature and salinity data are linearly interpolated onto 121 vertical levels from the surface to the depth of 1 200 m with an interval of 10 m using the Akima spline method (Akima, 1970). The ring-induced potential temperature (θ') and salinity (S') anomaly profiles were computed by removing monthly mean climatologic profiles of WOA13. For each ring, we search the float profiles located in the range of twofold radius and calculate the relative zonal and meridional distance, ΔX_E and ΔY_E, of floats to the eddy-center (which is defined at the position $\Delta X_E=\Delta Y_E=0$). All of the profiles are then used for composition. In addition, to eliminate the influence of radius on the composite result, ΔX_E and ΔY_E are divided by the corresponding radius R so that they are dimensionless. In addition, for a profile surfacing at the boundary of a ring, it shall also meet the condition $\sqrt{\Delta X_E^2 + \Delta Y_E^2} = 1$. Considering that a ring might not be perfectly circular in shape, the relative distance, ΔX_E and ΔY_E, of each profile are further normalized by the distance of the ring edge from the eddy center in the direction of the float. The floats are then classified into three categories: the profiles inside the cyclonic rings, those inside the anticyclonic rings, and those outside rings (Table 2).

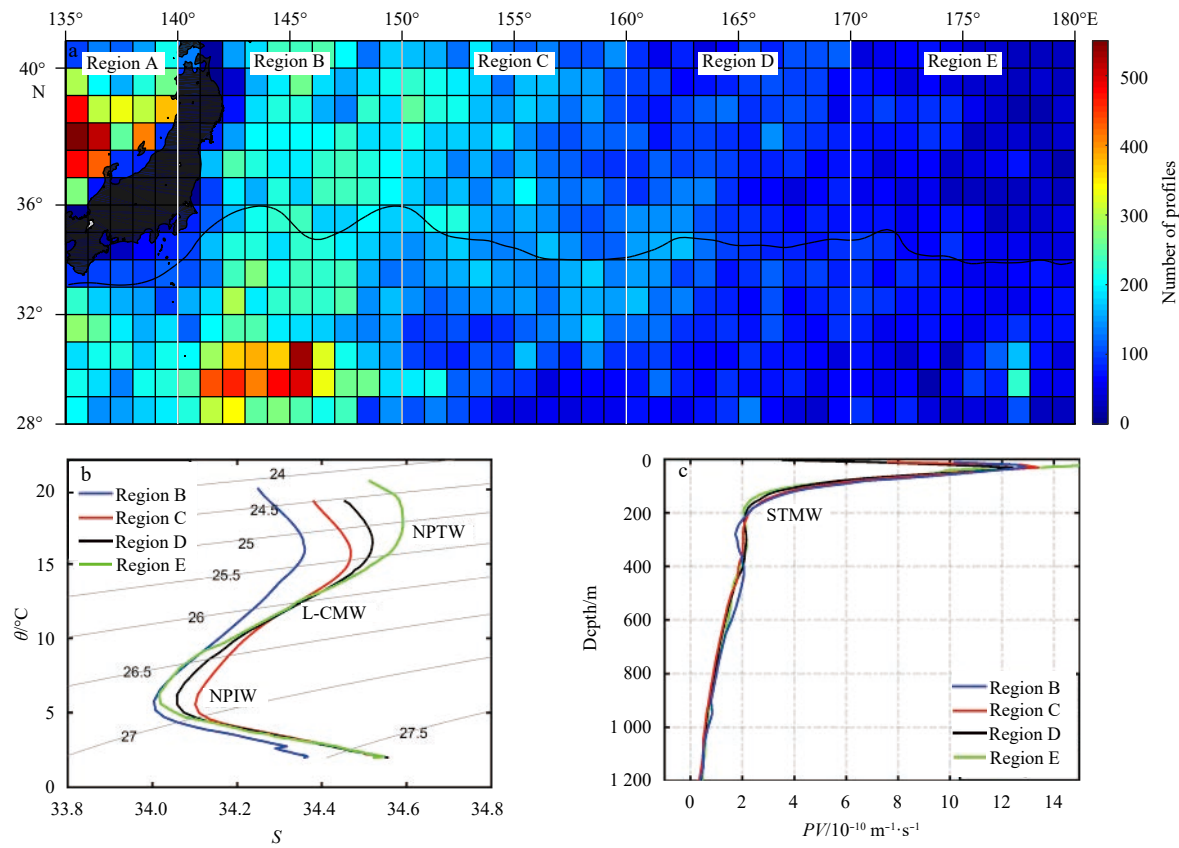It is concerned by Chaigneau et al. (2011) and Yang et al.

Fig. 2. Floats distribution and main water masses in the study regions. a. The spatial distribution of floats available in the KE region, with the number of floats shown in 1°×1° bin in the period 1999–2015; b. The mean potential temperature-salinity diagrams; and c. the mean potential vorticity (*PV*) diagrams for sub-regions B to E, calculated with all float profiles outside the eddies. NPTW: North Pacific Tropical Water; L-CMW: Lighter Center Mode Water; NPIW: North Pacific Intermediate Water; and STMW: Subtropical Mode Water.

Table 1. Statistics of the rings shed from the KE jet from 1993 to 2015

	Number		Amplitude/cm	Lifetime/d	radius/km
	all	reabsorbed			
Region B	160	87	34.9/37.6	52/60	96.7/82.5
Region C	169	113	33.9/37.3	43/69	103.9/92.4
Region D	139	87	28.5/34.0	42/43	109.1/102.4
Region E	49	35	25.3/29.7	46/37	116.0/109.5

Note: The data separated by a slash are those of the anticyclonic/cyclonic rings.

Table 2. The floats caught by rings and inside the range of twofold radius of rings in each sub-region

	Number	Floats caught by rings	Inside the range of twofold radius of rings	Outside rings
Region B	30 182	173/140	704/799	13 714
Region C	19 615	156/206	950/759	10 058
Region D	13 318	61/104	509/297	6 457
Region E	8 299	17/25	77/108	4 598

Note: The values separated by a slash are those of the anticyclonic rings/cyclonic rings.

(2013) that errors might arise from three potential causes in the classification of the floats. First, the accuracy of the location of the Argo profile depends on the precision of the Argo positioning system. Nevertheless, though the precision of the Argo positioning system varies from 0.1 to 1.0 km for different classes of floats, errors of this type are basically negligible in our study compared to the O (100 km) spatial scale of the ring. Second, the exact surfacing location of an Argo profile cannot be determined accurately, since there is a time lag (typically 1 hour) in the positioning of the satellite, during which the float is advected by the surface

current. In this scenario, the error between the reported Argo location and the surfacing location is actually small (<1 km) if we assume a mean surface current speed of 24 cm/s (Qiu and Chen, 2010) between 30°N and 40°N. The third potential cause is that the rings were identified from the daily ADT maps, rather than at the exact surfacing times reported by the Argo floats. Note that all the Argo profiles inside the ring usually were recorded 1.6 h behind the ring; therefore the maximum distance error is estimated to be 213 m since the mean propagation velocity of the ring is around 3.7 cm/s in the study region. Thus, the total distance er-

ror induced by the synchronization bias and the positioning error shall be around 2–3 km on average. Indeed, this may lead to a misclassification of an Argo profile, especially for those located very close to the eddy edge. However, this shall not be an issue in our study as we have only 0.5% of the profiles located closer than 2–3 km to the detected ring edges.

To obtain the ring-induced 3D θ' and S' structures in a specific sub-region, all θ' and S' profiles on the eddy-coordinate space $(\Delta X_E, \Delta Y_E)$ are mapped onto 0.1×0.1 grid using the objective analysis (Barth et al., 2014). Also, at each depth, anomaly data are treated as outliers and are removed if they are more than three times away from either the first or the third quartile. Thus, for each sub-region, one unique 3D θ'/S' ring composite structure can be obtained.

3.2 *Temperature structures*

Figure 3 shows the mean θ' diagrams of the composite rings in three sub-regions. Note that sub-region E is not included, considering few floats captured by the rings in this region. From the sub-regions B to C and then to D, the depths of extreme θ' caused by anticyclonic rings gradually deepen from about 180 m to 200 m and then to 400 m, whereas those caused by the cyclonic rings shoal from 600 m to 500 m and eventually to 400 m. The θ' induced by the composite anticyclonic ring can reach 3-4℃ in the main thermocline (regions B and C), which is much larger than that induced by the other eddies. The largest θ' values for both the anticyclonic and the cyclonic rings are found along the path of the KE jet between 140°E and 160°E. This is consistent with the results of Sasaki and Minobe (2015).

Figure 4 shows vertical sections of θ' of the composite anticyclonic and cyclonic rings at $\Delta Y = 0$ in sub-regions B, C and D. Albeit with some differences in detail, the composite anticyclonic (cyclonic) ring is characterized by an anomalously positive (negative) θ'. And the extreme value depths of both the anticyclonic and cyclonic rings as well as the intensity of the central θ' in different sub-regions vary widely. Consistent with the mean anomaly profiles (Fig. 3), moving from the sub-region B to D, the

maximum central depth of θ' becomes shallower for the cyclonic rings whereas it becomes deeper for the anticyclonic rings, with a gradually decreasing influence range. To explain this phenomenon, the depth of the zonal thermocline was compared with that of the maximum temperature anomaly of the rings. Figure 5 exhibits the mean vertical profiles of the potential temperature based on the outside eddies from the Argo profiles, with the depth of the main thermocline highlighted in a red frame. Clearly, the region B, which displayed the maximum temperature anomaly among the three sub-regions, demonstrated a much deeper main thermocline than the other two regions. Note that the main thermocline in region B occured at similar depth as the maximum temperature anomaly of rings. Therefore, it seems that the above deepening or shoaling trend is associated with the zonal change of the depth of the main thermocline.

The θ' pattern of the composite cyclonic ring in sub-region B clearly exhibits a double-core vertical structure: one core located in the upper 50 m, and the other at the depth between 400–800 m. This double-core structure is associated with the existence of the low-PV STMW in the main thermocline. The STMW separates the thermocline into an upper part (>19℃, <200 m) and a lower part (8–15℃, 350–800 m), and in both layers there are large vertical temperature gradients. However, different from the cyclonic rings, such a double-core structure is barely recognizable in the images of the anticyclonic rings. Such a difference between the composite cyclonic and anticyclonic rings can be partly explained by the interaction of the rings with the STMW. The doming of the isopycnal associated with the cyclonic rings tend to lift the upper thermocline more strongly than the lower thermocline (because eddy signals are stronger in the shallow water in general). Consequently, the upper thermocline is elevated with larger magnitude than the lower thermocline, which enlarges the thickness of the STMW. This effect leads to a better differentiated θ' in the two layers and a more defined double-core structure. On the contrary, the anomalous concave of the isopycnal associated with the anticyclonic rings make deepening trend more prominent for the upper thermocline; as a result, the thickness of the
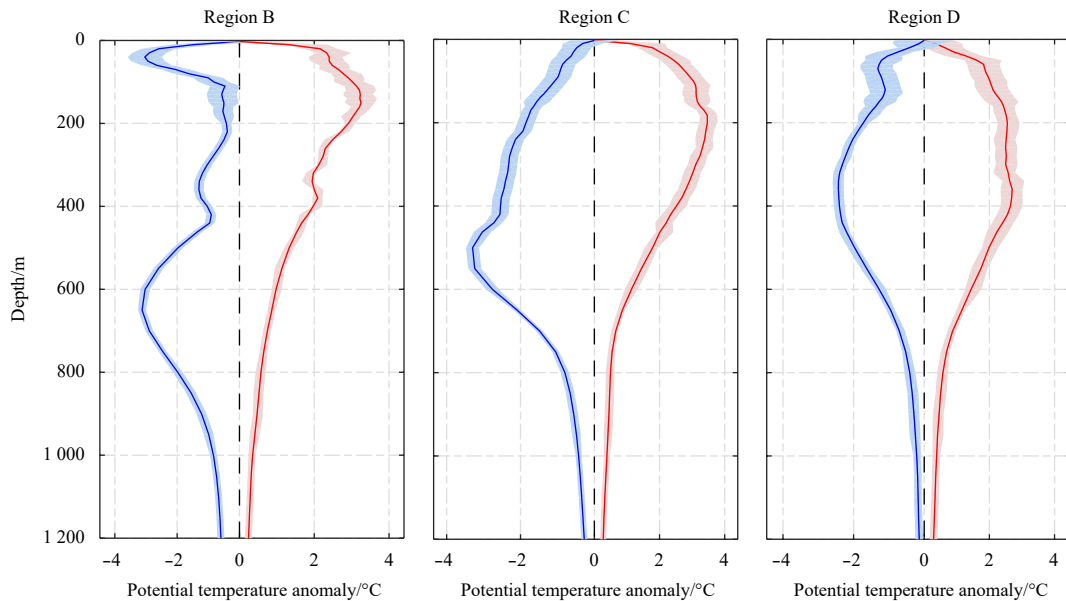

Fig. 3. The mean vertical profiles of potential temperature anomaly θ' (°C) for the anticyclonic and cyclonic rings in the three sub-regions. The blue and red curves in each diagram represent the anomaly for the cyclonic and anticyclonic rings, respectively. The shading indicates one standard deviation.
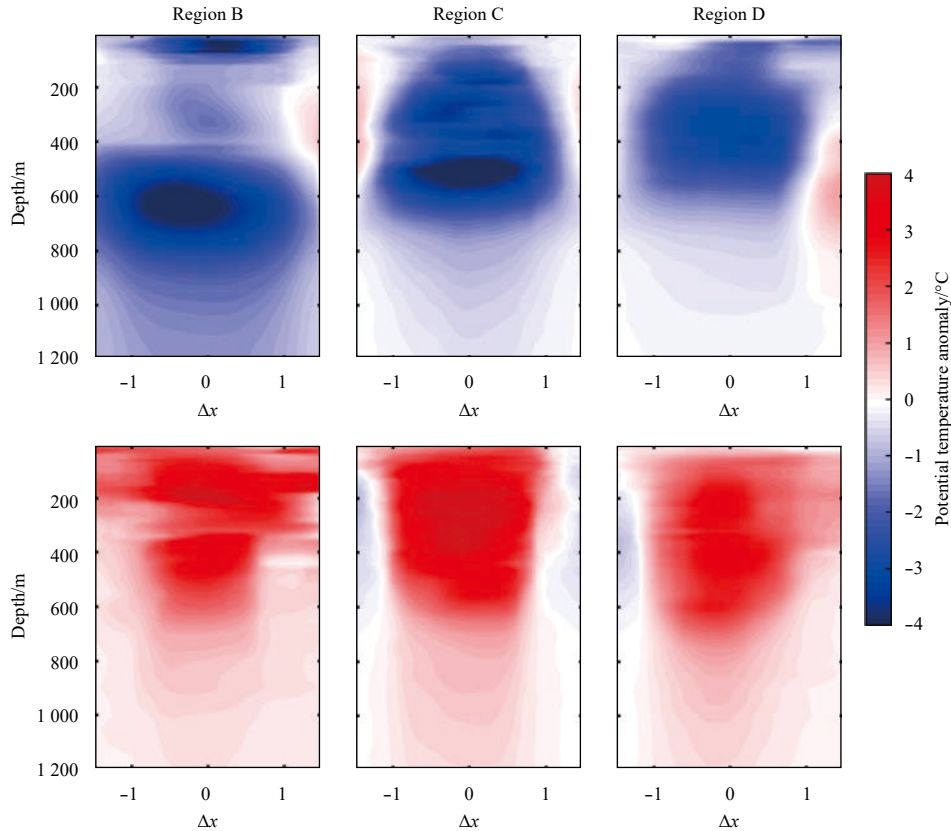
Fig. 4. Vertical sections of potential temperature anomaly (θ') of composite cyclonic (top) and anticyclonic (bottom) rings at $\Delta y = 0$ in sub-regions B, C, and D.
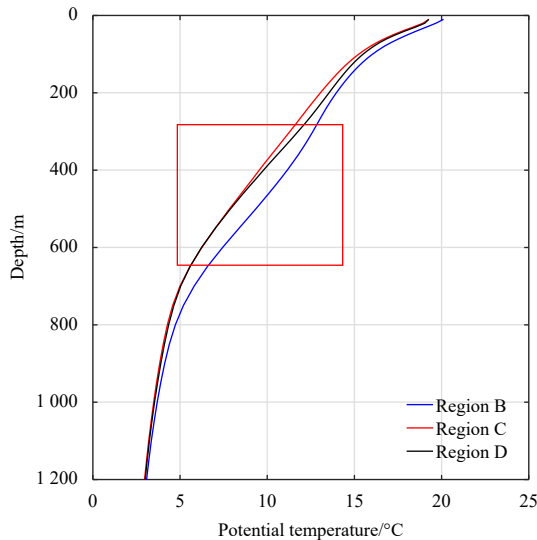

Fig. 5. Mean vertical profiles of potential temperature based on the profiles outside eddies. The frame in red indicates the depth of the main thermocline.

STMW would be compressed. Hence, instead of a double-core pattern, the two θ' cores would be barely disparted or even fused into a single one in the case of the anticyclonic ring. Similarly, in our study, the θ' core of the lower composite cyclonic ring was larger than that of the upper one, which may also be related to the STMW (which is a uniform and stable water mass). Due to the

doming of the isopycnal for cyclonic rings, the cold water would be gathered under the STMW, which therefore enabled the lower core more visible.

The lateral θ' structures at the depths of 10, 150, 300, 450, 600, 900, and 1 200 m are compared in Fig. 6. The θ' magnitude in the whole layer is small and distributed chaotically with contours disordered at 10 m. The θ' contours of the ring in each sub-region demonstrate an obvious enclosed structure. The maximum anomaly θ' magnitude occurs near the ring center at the depth of 400–600 m for the cyclonic ring and 150–450 m for the anticyclonic ring. Below these two depths, the magnitude drops quickly, though their structures are well maintained till the depth of 900 m where the maximum θ' magnitude is –0.4°C and 0.2°C for the cyclonic and anticyclonic ring, respectively.

3.3 *Salinity structures*

The mean vertical profiles of salinity anomaly S' for anticyclonic and cyclonic rings in three sub-regions are further depicted in Fig. 7. Some abnormally small peaks in the surface layer could be found, probably due to the usage of more float data. Above 600 m the anticyclonic (cyclonic) rings exhibited a relatively large positive (negative) S'; and the core with maximum positive (minimum negative) anomaly of the anticyclonic ring gradually deepens (shoals) from 200 to 400 m (from 400 to 300 m) in sub-regions B, C, and D. Below 600 m, a relatively small negative (positive) S' was observed for the anticyclonic (cyclonic) ring; and the core with the maximum positive anomaly of the cyclonic ring gradually shrank from 800 to 700 m in three sub-regions, whereas little changes occurred in the core with the maximum negative anomaly of anticyclonic rings. It shall be mentioned that an
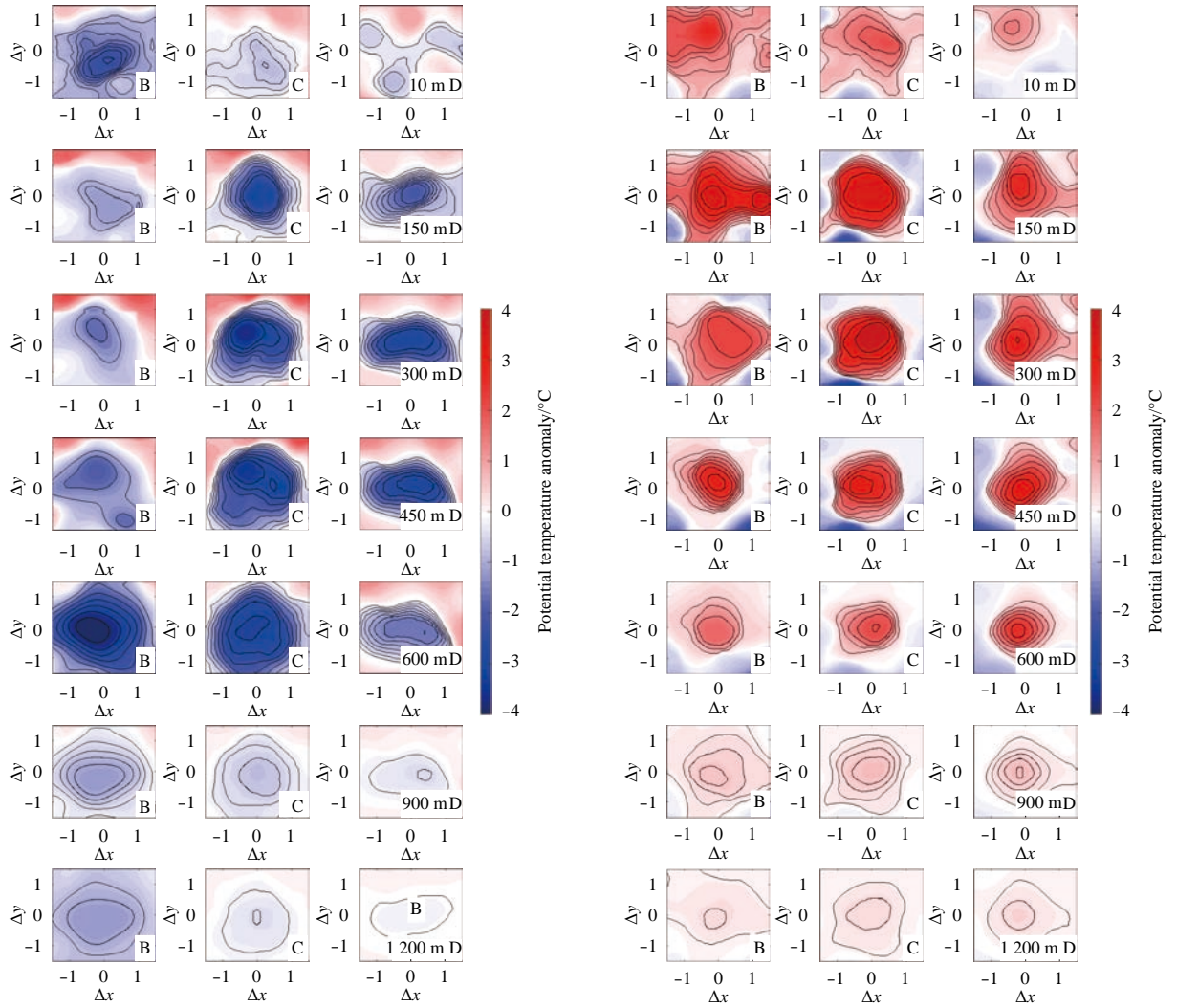
Fig. 6. Horizontal distributions of potential temperature anomaly (θ') of the composite cyclonic rings (the left three columns) and anticyclonic rings (the right three columns) at depths of 10, 150, 300, 450, 600, 900, and 1 200 m in sub-regions B, C, and D, respectively.
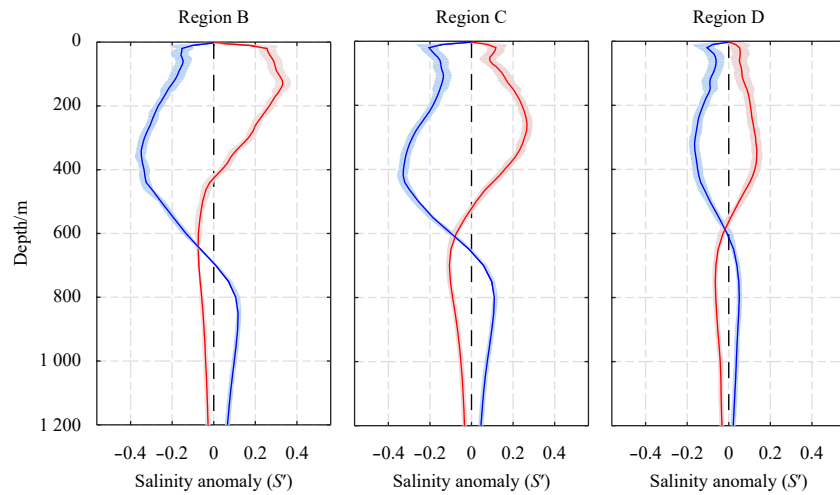

Fig. 7. Mean vertical profiles of salinity anomaly (S') for anticyclonic and cyclonic rings in all sub-regions. The blue and red curves represent the anomaly for the cyclonic and anticyclonic rings, respectively. Shading indicates one standard deviation.

eastward weakening of ring signals with largest S' magnitude for both anticyclonic and cyclonic rings found in sub-regions B and C. Such results agree well with the results of Sasaki and Minobe (2015).

The vertical distribution of the water masses is an important factor in determining the S' pattern, which interacts with the vertical motion of a ring to construct S'. The vertical sections of S' of the composite rings at $\Delta y = 0$ are shown in Fig. 8. The interior of the cyclonic ring presents a "negative-positive" S' structure in the upper-lower layers whereas an opposite structure, i.e., a "positive-negative" S', was observed for the upper-lower layers in the anticyclonic rings. The depth of 600 m and 580 m roughly define the boundary of the positive and the negative anomaly, respectively. The reason for the formation of this S' structure is associated with the salinity inside the ring which has a minimum value at the depth of about 600 m. Specifically, inside the cyclonic ring, due to the doming of the isopycnal, the higher salinity water mass (NPTW) above 600 m was thus replaced by the lower salinity water mass (NPIW), resulting in a negative S' in the upper layer; in the meanwhile, the deep signature of the cyclonic ring enabled a positive S' in the lower portion of the NPIW by lifting up the relatively saltier NPDW. Note that the positive S' is smaller than 0.1 psu, due to the decreasing ring signals and vertical salinity gradients in this layer. For the anticyclonic ring, the concave of the isopycnal inside lead to the opposite anomaly distribution of salinity; accordingly, the deepening of the NPTW produces a large positive S' in the entire subsurface layer and a small negative S' in the deeper layer (Yang et al., 2013).

For the cyclonic rings, from sub-region B to C to D, the minimum negative S' values of the upper-layer salinity were –0.36,

–0.34, and –0.19, while the maximum positive S' values of the lower-layer salinity are 0.13, 0.10, and 0.05, respectively. For the anticyclonic rings, the maximum positive S' values of the upper-layer salinity are 0.31, 0.25, and 0.12 from sub-region B to C to D, while the minimum negative S' values of the lower-layer are –0.08, –0.10, and –0.06, respectively. S' is generally larger in the regions of B and C.

Figure 9 depicts the horizontal distributions of S' of the composited cyclonic and anticyclonic rings at different depths from 10 m to 1 200 m in sub-regions B, C and D. The contour of S' distributed chaotically at 10 m. Going down from the depth of 450 m to 650 m, the S' of cyclonic rings changes from negative to positive while that of the anticyclonic transformed from positive to negative, which is consistent with the distribution of the salinity anomaly in Fig. 7. The S' existed obviously in each sub-region, though its magnitude decreased gradually up to the depth of 1 200 m. The overall horizontal scale of S' is larger than that of θ', which may be due to the slight salinity change caused by the rings and the small salinity differences between the water masses inside and outside the rings.

4 Summary and discussion

We provide a comprehensive description of statistical characteristics and 3D structures of the rings shed from the KE, using the AVISO multi-satellite altimetric ADT data from 1993 to 2015, the Argo temperature/salinity float profiles from the Ifremer, and the JAMSTEC cruise and buoy data. In total, 276 anticyclonic rings and 242 cyclonic rings shed from the KE jet were identified during the AVISO observation period using the manual eddy detection method. Our results reveal that the cyclonic rings main-
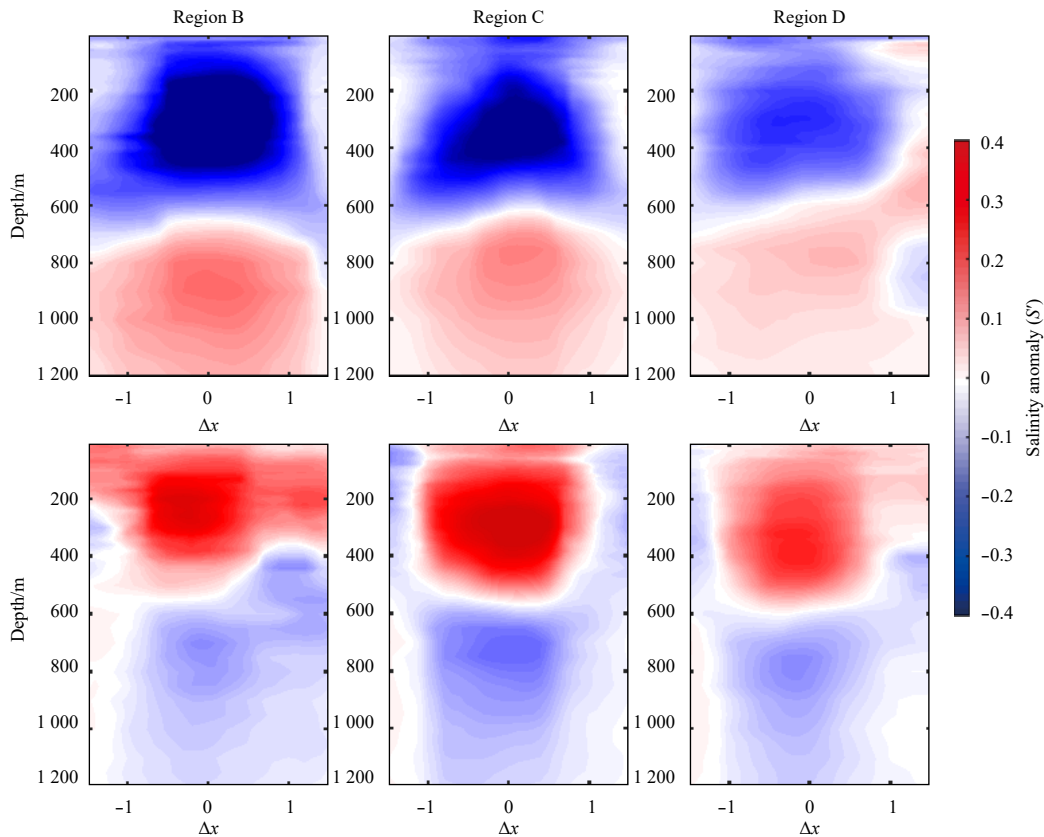

Fig. 8. Vertical sections of salinity anomaly (S') of the composite cyclonic rings (top) and the anticyclonic rings (bottom) at $\Delta y = 0$ in sub-regions B, C, and D.
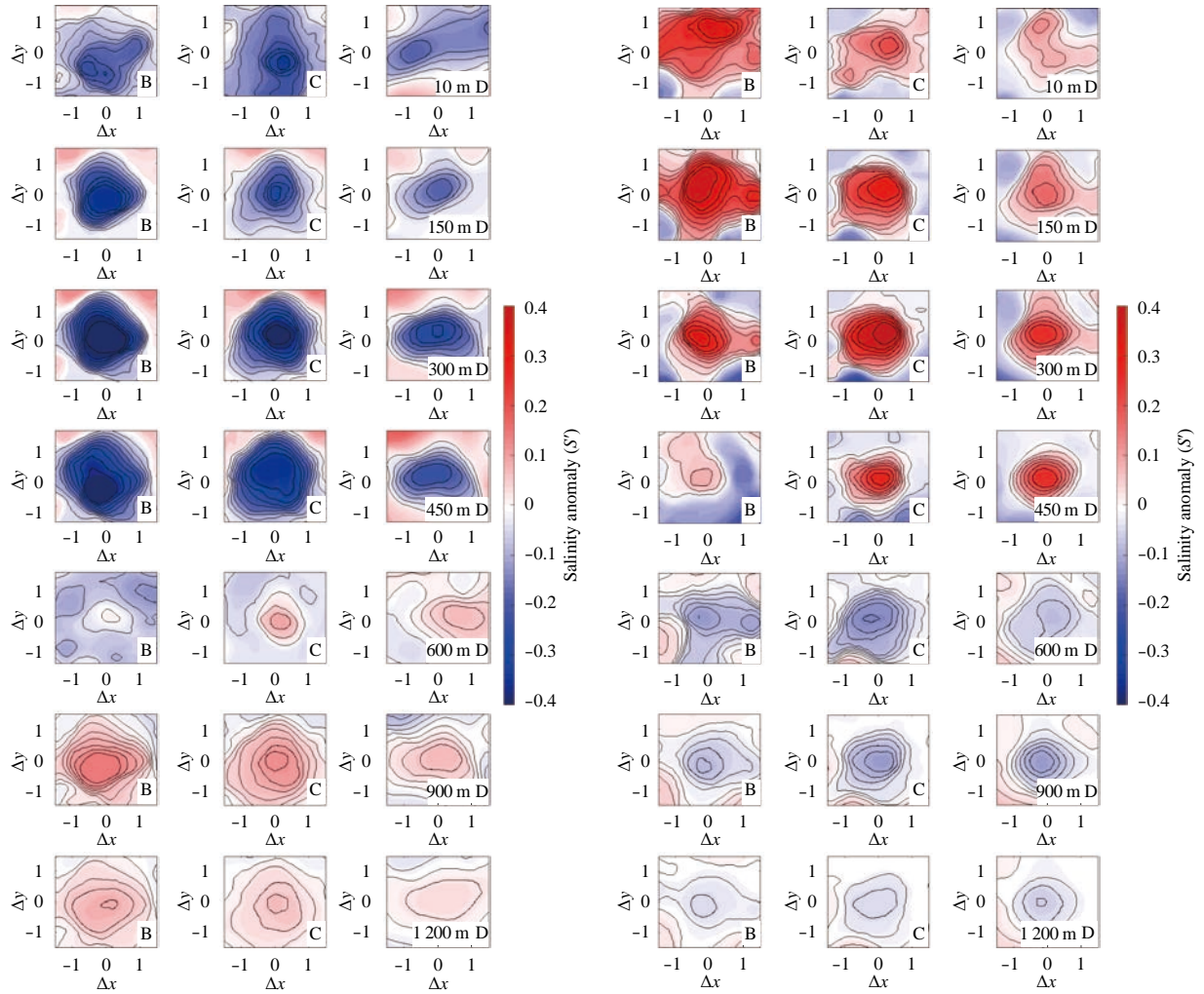
Fig. 9. Horizontal distributions of salinity anomaly (S') of composited cyclonic rings (the three left columns) and anticyclonic rings (the three right columns) at depths of 10, 150, 300, 450, 600, 900, and 1 200 m in sub-regions B, C, and D.

tained obvious negative θ' and its maximum anomaly depth became increasingly shallow along with θ' decreasing from the west to the east; accordingly, the anticyclonic ones demonstrated persistently positive θ', and its maximum anomaly depth went deeper with decreasing θ' from the west to the east. According to our research, it seems that the above deepening or shoaling trend is associated with the zonal change of the depth of main thermocline. The θ' induced by the composite anticyclonic ring could reach 3–4 ℃ in the main thermocline in sub-regions B and C, much larger than those induced by other eddies. Due to the existence of low-PV STMW in the main thermocline, the θ' pattern of the composite cyclonic ring in sub-region B exhibited a well-defined double-core vertical structure, with one core located at the depth of 50 m and the other between 400–800 m. However, such a double-core structure was barely discernible in the anticyclonic rings. Such a structural difference between the cyclonic and anticyclonic rings could be partly explained by their interaction with the STMW. The doming of the isopycnal associated with the cyclonic rings; and the cyclonic ring itself tends to lift the upper thermocline more than the lower thermocline (because eddy signals are generally strong in the shallow water). In this scenario, the upper thermocline thus would be elevated much higher than the lower thermocline, which thus enlarges the thickness of the STMW. This effect hence differentiates the value of θ' in the

two layers, leading to the generation of a double-core structure. Instead, the concave of the isopycnal for the anticyclonic ring together with a more prominent deepening effect on the upper thermocline, compresses the thickness of the STMW. Consequently, the two θ' cores were barely aparted or even fused into a single core.

The boundary of the positive and negative S' anomaly was estimated to occur at the depth of 600 m and 580 m, respectively. Above 600 m, for the anticyclonic ring, a relatively large positive S' was observed, and the core with the maximum positive anomaly gradually deepens from 200 to 400 m; for the cyclonic rings, they exhibited a negative S', and the core with the minimum negative anomaly shrank from 400 m to 300 m in sub-regions B, C, and D. Below 600 m, the anticyclonic ring had a relatively small negative S', which exhibited no signnificant changes along with the depth; for the cyclonic ring a small positive S' was found and the core with a maximum positive anomaly gradually shoals from 800 to 700 m in sub-regions B, C, and D. Such a S' structure is closely associated with the vertical distribution of water mass which interacts strongly with the ring. Specifically, the minimum salinity inside the ring occurred at around the depth of 600 m; the higher salinity water mass (NPTW) above 600 m was replaced by the lower salinity water mass (NPIW) owing to the doming of the isopycnal inside the cyclonic ring, resulting in a negative S' in the

upper layer, while a positive S' in the lower portion of the NPIW was generated as the cyclonic ring with deep signature could uplift the relatively saltier NPDW. For the anticyclonic ring, in comparison, the concave of the isopycnal inside caused the opposite anomaly distribution of salinity; the deepening of the NPTW produced large positive S' in the entire subsurface layer but small negative S' in the deeper layer.

In general, the influences on the temperature and salinity anomaly of the composite rings vary spatially, which may be related to the intensity of the background current and the temperature and salinity fields in each sub-region. The influence of the rings on the temperature and salinity could reach more than 1 000 m in terms of the average depth.

The large θ'/S' values of the rings revealed in this study indicate considerable transports (Roemmich and Gilson, 2001; Qiu and Chen, 2005; Chen et al., 2012) of heat and salt in the KE region, which is the focus of our ongoing research. The vertical structures of these rings under pronounced variations of ocean background conditions (Qiu and Chen, 2010; Rudnick et al., 2011) and their influence on the STMW in the relevant region is also interesting, which will be addressed in our furture follow-up study.

References

Akima H. 1970. A new method of interpolation and smooth curve fitting based on local procedures. Journal of the ACM, 17(4): 589–602, doi: 10.1145/321607.321609

Barth A, Beckers J M, Troupin C, et al. 2014. Divand-1.0: n-dimensional variational data analysis for ocean observations. Geoscientific Model Development, 7(1): 225–241, doi: 10.5194/gmd-7-225-2014

Chaigneau A, Gizolme A, Grados C. 2008. Mesoscale eddies off Peru in altimeter records: Identification algorithms and eddy spatio-temporal patterns. Progress in Oceanography, 79(2–4): 106–119, doi: 10.1016/j.pocean.2008.10.013

Chaigneau A, Le Texier M, Eldin G, et al. 2011. Vertical structure of mesoscale eddies in the eastern South Pacific Ocean: A composite analysis from altimetry and Argo profiling floats. Journal of Geophysical Research: Oceans, 116(C11): C11025, doi: 10.1029/2011JC007134

Chelton D B, Schlax M G, Samelson R M, et al. 2007. Global observations of large oceanic eddies. Geophysical Research Letters, 34(15): L15606, doi: 10.1029/2007GL030812

Chelton D B, Schlax M G, Samelson R M. 2011. Global observations of nonlinear mesoscale eddies. Progress in Oceanography, 91(2): 167–216, doi: 10.1016/j.pocean.2011.01.002

Chen Gengxin, Gan Jianping, Xie Qiang, et al. 2012. Eddy heat and salt transports in the South China Sea and their seasonal modulations. Journal of Geophysical Research: Oceans, 117(C5): C05021, doi: 10.1029/2011JC007724

Cushman-Roisin B. 1993. Trajectories in Gulf Stream meander. Journal of Geophysical Research: Oceans, 98(C2): 2543–2554, doi: 10.1029/92JC02059

Ding Ya′nan, Jing Chunsheng, Qiu Yun. 2019. Temporal and spatial characteristics of pinch-off rings in the Kuroshio Extension re-
gion. Haiyang Xuebao (in Chinese), 41(5): 47–58, doi: 10.3969/j.issn.0253-4193.2019.05.005

Dong Di, Brandt P, Chang Ping, et al. 2017. Mesoscale eddies in the Northwestern Pacific Ocean: three-dimensional eddy structures and heat/salt transports. Journal of Geophysical Research: Oceans, 122(12): 9795–9813, doi: 10.1002/2017JC013303

Faghmous J H, Frenger I, Yao Yuanshun, et al. 2015. A daily global mesoscale ocean eddy dataset from satellite altimetry. Scientific Data, 2: 150028, doi: 10.1038/sdata.2015.28

Itoh S, Yasuda I. 2010. Characteristics of mesoscale eddies in the Kuroshio-Oyashio Extension Region detected from the distribution of the sea surface height anomaly. Journal of Physical Oceanography, 40(5): 1018–1034, doi: 10.1175/2009JPO4265.1

Japan Agency for Marine-Earth Science and Technology. 2016. Data and Sample Research System for Whole Cruise Information in JAMSTEC (DARWIN). http://www.godac.jamstec.go.jp/darwin/ [2018-09-17]

Jochumsen K, Rhein M, Hüttl‐Kabus S, et al. 2010. On the propagation and decay of North Brazil Current rings. Journal of Geophysical Research: Oceans, 115(C10): C10004, doi: 10.1029/2009JC006042

Kouketsu S, Tomita H, Oka E, et al. 2012. The role of meso-scale eddies in mixed layer deepening and mode water formation in the western North Pacific. Journal of Oceanography, 68(1): 63–77, doi: 10.1007/s10872-011-0049-9

Martin A P, Richards K J. 2001. Mechanisms for vertical nutrient transport within a North Atlantic mesoscale eddy. Deep-Sea Research, Part II: Topical Studies in Oceanography, 48(4–5): 757–773, doi: 10.1016/S0967-0645(00)00096-5

Masuzawa J. 1969. Subtropical mode water. Deep Sea Research and Oceanographic Abstracts, 16(5): 463–472, doi: 10.1016/0011-7471(69)90034-5

McGillicuddy D J Jr, Anderson L A, Bates N R, et al. 2007. Eddy/wind interactions stimulate extraordinary mid-ocean plankton blooms. Science, 316(5872): 1021–1026, doi: 10.1126/science.1136256

Mcwilliams J C, Flierl G R. 1979. On the evolution of isolated, nonlinear vortices. Journal of Physical Oceanography, 9(9): 1155–1182

Olson D B. 1991. Rings in the ocean. Annual Review of Earth and Planetary Sciences, 19(1): 283–311, doi: 10.1146/annurev.ea.19.050191.001435

Qiu Bo. 2000. Interannual variability of the Kuroshio Extension system and its impact on the wintertime SST field. Journal of Physical Oceanography, 30(6): 1486–1502, doi: 10.1175/1520-0485(2000)030<1486:IVOTKE>2.0.CO;2

Qiu Bo. 2003. Kuroshio extension variability and forcing of the pacific decadal oscillations: responses and potential feedback. Journal of Physical Oceanography, 33(12): 2465–2482, doi: 10.1175/2459.1

Qiu Bo, Chen Shuiming. 2005. Eddy-induced heat transport in the subtropical North Pacific from Argo, TMI, and altimetry measurements. Journal of Physical Oceanography, 35(4): 458–473, doi: 10.1175/JPO2696.1

Qiu Bo, Chen Shuiming. 2010a. Interannual variability of the North Pacific Subtropical Countercurrent and its associated mesoscale eddy field. Journal of Physical Oceanography, 40(1): 213–225, doi: 10.1175/2009JPO4285.1

Qiu Bo, Chen Shuiming. 2010b. Eddy-mean flow interaction in the decadally modulating Kuroshio Extension system. Deep Sea Research Part II: Topical Studies in Oceanography, 57(13–14): 1098–1110, doi: 10.1016/j.dsr2.2008.11.036

Roemmich D, Gilson J. 2001. Eddy transport of heat and thermocline waters in the north pacific: a key to interannual/decadal climate variability. Journal of Physical Oceanography, 13(3): 675–688, doi: 10.1175/1520-0485(2001)031<0675:ETOHAT>2.0.CO;2

Rudnick D L, Jan S, Centurioni L, et al. 2011. Seasonal and mesoscale variability of the Kuroshio near its origin. Oceanography, 24(4): 52–63, doi: 10.5670/oceanog.2011.94

Sasaki Y N, Minobe S. 2015. Climatological mean features and interannual to decadal variability of ring formations in the Kuroshio

Extension region. Journal of Oceanography, 71(5): 499–509, doi: 10.1007/s10872-014-0270-4

Souza J M A C, De Boyer Montégut C, Cabanes C, et al. 2015. Estimation of the Agulhas ring impacts on meridional heat fluxes and transport using ARGO floats and satellite data. Geophysical Research Letters, 38(21): L21602

Suga T, Hanawa K, Toba Y. 2010. Subtropical mode water in the 137°E section. Journal of Physical Oceanography, 19(10): 1605–1619

Suga T, Kato A, Hanawa K. 2000. North Pacific Tropical Water: its climatology and temporal changes associated with the climate regime shift in the 1970s. Progress in Oceanography, 47(2–4): 223–256, doi: 10.1016/S0079-6611(00)00037-9

Talley L D. 1993. Distribution and formation of North Pacific Intermediate Water. Journal of Physical Oceanography, 23(3): 517–537, doi: 10.1175/1520-0485(1993)023<0517:DAFONP> 2.0.CO;2

Waterman S, Hoskins B J. 2013. Eddy Shape, orientation, propagation, and mean flow feedback in Western Boundary Current jets. Journal of Physical Oceanography, 43(8): 1666–1690, doi: 10.1175/JPO-D-12-0152.1

Yang Guang. 2013. A study on the mesoscale eddies in the Northwestern Pacific Ocean (in Chinese) [dissertation]. Qingdao: The Institute of Oceanology, Chinese Academy of Sciences

Yang Guang, Wang Fan, Li Yuanlong, et al. 2013. Mesoscale eddies in the northwestern subtropical Pacific Ocean: Statistical characteristics and three-dimensional structures. Journal of Geophysical Research: Oceans, 118(4): 1906–1925, doi: 10.1002/jgrc. 20164

Zhang Ronghua, Rothstein L M, Busalacchi A J. 1998. Origin of upper-ocean warming and El Nino change on decadal scales in the tropical Pacific Ocean. Nature, 39(6670): 879–883